


Experimental observation of the topological interface state in a one-dimensional waterborne acoustic waveguide

Licheng Luo¹, Liping Ye¹, Hailong He¹, Jiuyang Lu^{1,*}, Manzhu Ke^{1,†} and Zhengyou Liu^{1,2}

¹Key Laboratory of Artificial Micro- and Nano-structures of Ministry of Education and School of Physics and Technology, Wuhan University, Wuhan 430072, China

²Institute for Advanced Studies, Wuhan University, Wuhan 430072, China

 (Received 6 July 2023; revised 3 September 2023; accepted 6 September 2023; published 4 October 2023)

Topological insulators that exhibit localized states at the edges or interference regions have been extensively investigated. Among these, waterborne acoustic topological interface states have significant potential in applications such as particle manipulation. However, the large impedance of water can no longer be ignored and sets difficulty in the construction of the waveguide in observing the topological states. In this paper, we propose an effective strategy to circumvent this issue and achieve the direct observation of the topological interface state in a waterborne acoustic waveguide as well as the associated nonzero Zak phases. Moreover, the robustness of the interface state against disorder is validated, suggesting a viable method for studying underwater topological acoustic fields.

DOI: [10.1103/PhysRevApplied.20.044008](https://doi.org/10.1103/PhysRevApplied.20.044008)

I. INTRODUCTION

Originating from the context of the quantum Hall effect, the concept of the topological insulator has generated considerable recent research interest [1]. The most attractive point is the existence of topologically protected localized states in the lower-dimensional boundaries, which is guaranteed by bulk-boundary correspondence and is robust to imperfections [2–6]. Based on the common properties of wave motion, topological states can be extended to various classical wave systems, such as photonics [7–9], mechanics [10–12], and acoustics [13–17], in which the localized states have potential in controlling the propagation of classical waves. Among these classical waves, the acoustic wave, especially the waterborne acoustic wave, is interesting for its potential application in noncontact particle manipulation [18–22], such as achieving medicine transport and disease therapy [23].

To achieve topological states of waterborne acoustic waves, the simplest and typical Su-Schrieffer-Heeger (SSH) model [24] is adopted. This is a one-dimensional (1D) lattice that contains two different components in its periodic unit cell and exhibits localized states at the end of the topologically nontrivial phase or the interface between two topologically distinct phases. The phase in the SSH model is described by the Zak phase, which is a property

arising from the bulk, and has the value of 0 or π for the topologically trivial or nontrivial phase. A conventional strategy for constructing the SSH model in airborne acoustics is to resort the cavity-tube structure [25–28], with the resonance cavities and tubes mapped to the sublattice sites and couplings in the SSH model. Another approach is based on the continuous case, including the multi-layer system composed of materials with different acoustic impedances [29,30], or the waveguide system composed of segments with different geometrical sizes [31–34]. The dispersion relationship of both systems can be obtained by the continuity condition between the layers or segments. However, such a strategy no longer works for waterborne acoustic waves because the impedance of water can no longer be ignored (compared with the airborne scenarios), and consequently the acoustically rigid resonance cavities and tubes cannot be well constructed in a background of water.

In this work, we realize a topological interface state in a 1D waterborne acoustic waveguide. The waveguide is constructed using segments with different widths, and, to further confine waves in the waveguide, a 2D steel-air metastructure is designed in the walls of the waveguide. We observe the topological interface state and experimentally detect the nonzero Zak phase as the topological invariant to protect the interface state. We further introduce disorder in the experiment to verify the robustness of the interface states. Our research demonstrates that the waterborne acoustic waveguide maintains its topological property at high frequency, providing a platform for constructing the topological states in water.

*jylu@whu.edu.cn

†mzke@whu.edu.cn

II. METHODS

We consider the unit cell of the acoustic waveguide shown in Fig. 1(a). Here we show that it can map to the SSH model. The acoustic waveguide is composed of segments with the same length l_0 and two different widths S_A and S_B . The acoustic wave propagates along the x direction. Focusing on the monopole mode, the acoustic pressure field is governed by the 1D Helmholtz equation $d^2p/dx^2 + k^2p = 0$, where the wave vector $k = 2\pi f/c_w$ relates to the operational frequency f and the sound velocity in water $c_w = 1490$ m/s. For the points where the width of the waveguide changes abruptly, the acoustic pressure and flow rate are continuous, which requires $p^+(x) = p^-(x)$ and $S^+ dp^+(x)/dx = S^- dp^-(x)/dx$, with the superscript $+$ ($-$) denoting the right (left) side of the points. Taking the point A with coordinate x_n^A (n represents the n th unit cell) as an example, the fields at its two neighboring points B with coordinates x_{n-1}^B and x_n^B are related to that at point A by the following equations: $p(x_n^B) = p^+(x_n^A + l_0) = \cos(kl_0)p^+(x_n^A) + \sin(kl_0)k^{-1}dp^+(x_n^A)/dx$ and $p(x_{n-1}^B) = p^-(x_n^A - l_0) = \cos(kl_0)p^-(x_n^A) - \sin(kl_0)k^{-1}dp^-(x_n^A)/dx$. Here the second equality holds since the general solutions in each segment are expressed in trigonometric functions. Combining the above equations with the continuity conditions, one obtains $t_{AP}(x_n^B) + t_{BP}(x_{n-1}^B) = Ep(x_n^A)$, where $t_{A(B)} = S_{A(B)}/(S_A + S_B)$ and $E = \cos(2\pi f l_0/c_w)$. Similarly, $t_{AP}(x_n^A) + t_{BP}(x_{n+1}^A) = Ep(x_n^B)$ for the point B . Therefore, we have built the relations between the acoustic pressure at the points where the width of the waveguide changes. These points can directly map to the sublattice sites in the SSH model [blue and red dots in Fig. 1(a)] with $t_{A(B)}$ and E being the hoppings and energy, respectively [35]. Based on the band structures of the SSH model, i.e., $E = \pm\sqrt{t_A^2 + t_B^2 + 2t_A t_B \cos(2kl_0)}$, the analytical dispersions of the acoustic waveguide are plotted as the blue curves in Fig. 1(a), in comparison to the simulated results (using the finite-element analysis software COMSOL Multiphysics) denoted by red curves. The analytical dispersions repeat with the increase of frequency and coincide well with simulated ones from the first to the fifth band. As the frequency increases, the wavelength in water is no longer much larger than the width of the waveguide and the 1D approximation is gradually broken, resulting in a considerable difference between the analytical and simulated results in the sixth band. Nevertheless, the band gap between the fifth and sixth bands, ranging from 0.319 to 0.336 MHz, is still a typical gap in the SSH model, and this frequency range is compatible with our experimental measurement conditions.

Since the impedance of water cannot be ignored when compared to general solid materials, a 2D steel-air metastructure is designed to screen solid modes [36,37]. The unit cell of the metastructure is schematically shown in Fig. 1(b), together with its dispersions. The parameters

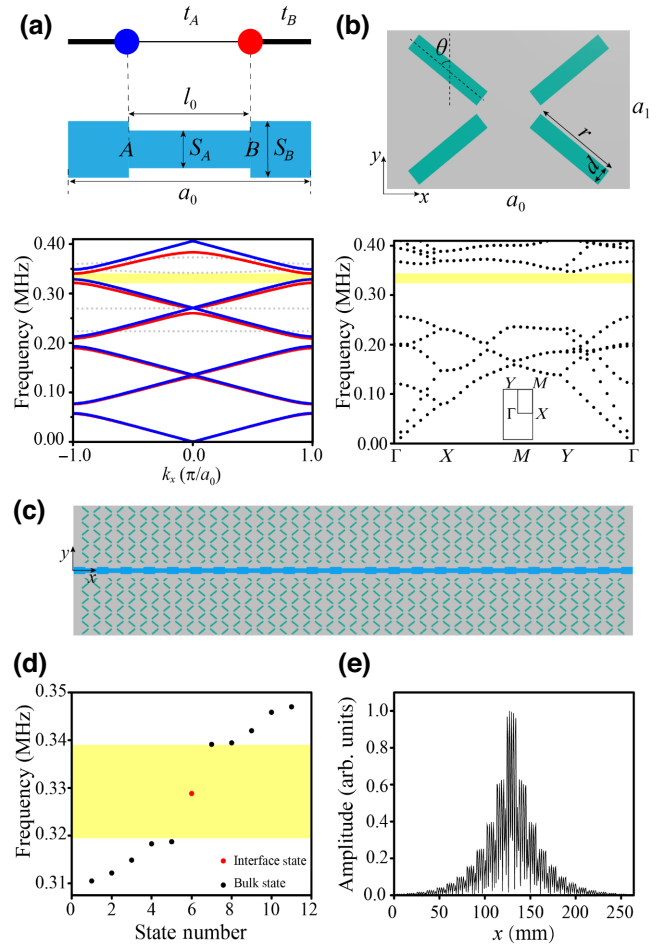


FIG. 1. (a) Upper panel: Schematic of the unit cell of the acoustic waveguide, which can map to an SSH model. The structure parameters are $S_A = 2.2$ mm, $S_B = 3.5$ mm, $a_0 = 11$ mm, and $l_0 = a_0/2$. Lower panel: The corresponding calculated (blue curves) and simulated (red curves) dispersions of the acoustic waveguide. The gray dots represent the high-order modes in the waveguide. (b) Upper panel: Schematic of the unit cell for the metastructures in the waveguide walls. Lower panel: The corresponding simulated dispersions of the metastructure. The structure parameters are $a_1 = 7$ mm, $r = 4.0$ mm, $d = 0.8$ mm, and $\theta = 51^\circ$. In (a),(b), the gray, green, and blue areas represent steel, air, and water, and the yellow regions denote the common band gap. (c) Schematic of the supercell with an interface. The origin is set at the left edge of the waveguide. For the left side $S_A = 2.2$ mm and $S_B = 3.5$ mm, while for the right side $S_A = 3.5$ mm and $S_B = 2.2$ mm. (d) Eigenfrequency spectra of the supercell. The red dot denotes the interface state. (e) Amplitude distribution of the interface state along the center line of the waveguide.

are as follows: for the solid material made by 316L stainless steel, the Young's modulus $E = 190$ GPa, the Poisson ratio $\nu = 0.26$, and the mass density $\rho_s = 8000$ kg/m³; and for air, the sound velocity $c_a = 343$ m/s, and the mass density $\rho_a = 1.29$ kg/m³. The band gap in such a metastructure can be adjusted by the rotation angle θ of the

air slot. When $\theta = 51^\circ$, a band gap opens and ranges from 0.257 to 0.348 MHz, which completely covers the band gap of the water waveguide. The impedance of the metastructure, owing to its omnidirectional band gap, mismatches that of water, thus providing perfect protection to the waterborne modes in the waveguide.

As shown in Fig. 1(c), by connecting two periodic acoustic waveguides of different topologies, we build the supercell with an interface, where acoustic waves propagate in the waveguide along the x direction. The total length of the supercell is 264 mm. The eigenfrequency of the supercell obtained by simulation is plotted in Fig. 1(d), where the bulk and interface states are marked by black and red dots, respectively. The interface state occurs within the band gap at the frequency of 0.329 MHz. Its amplitude distribution along the central line of the waveguide is plotted in Fig. 1(e), which is highly localized and exhibits exponential decay away from the interface.

III. RESULTS AND DISCUSSION

To experimentally observe the waterborne interface state, we fabricate the waveguide by using a 3D-metal-printing method. The sample is shown in Fig. 2(a). The upper face of the sample is sealed to construct air slots. The height of the sample is 75 mm in the z direction, much larger than the operational wavelength (about 4.8 mm), providing an ideal platform to observe the wave propagations along the x direction. Figure 2(b) shows the experimental setup. The ultrasonic transducer has a central frequency of 0.5 MHz and a diameter of 25 mm, and is placed 40 mm away from the left edge to offer a plane-wave incidence. In experiment, with a pulse (with time

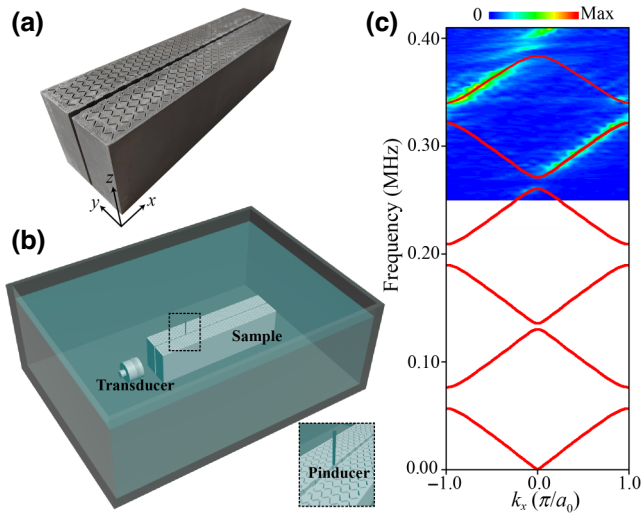


FIG. 2. (a) Photograph of the 3D-metal-printed sample. (b) Schematic of the experimental setup. (c) Band dispersions along the k_x direction of the waveguide. The color maps and red curves represent the experimental and simulated results, respectively.

duration $10 \mu\text{s}$) repeatedly sent from the transducer, the frequency-dependent acoustic fields along the waveguide are scanned by a pinducer. The diameter of the pinducer is 1.9 mm, slightly smaller than the width of the waveguide, which only permits the pinducer to scan along the x direction. Meanwhile, it detects the time-domain signals and transforms them into the frequency domain. By further Fourier transforming the frequency-dependent acoustic fields into momentum space, the measured dispersions of the waveguide are obtained and shown by color maps in Fig. 2(c), capturing the simulated dispersions of the positive propagation modes.

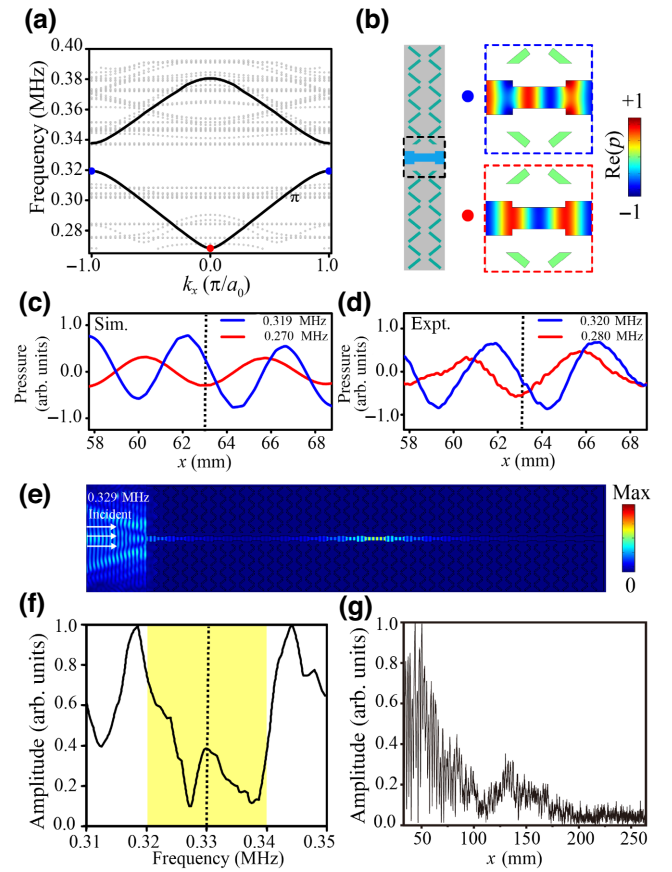


FIG. 3. (a) Band structure simulated for the unit cell consisting of the waveguide and the metastructure walls. The black curves represent the monopole waveguide mode while the gray dots denote other modes, including the high-order waveguide modes in water and modes in the metastructure. (b) Left panel: Schematic of the unit cell. Right panel: Simulated field distributions for the band-edge states marked by red and blue dots in (a). (c),(d) Simulated and measured pressure fields in one unit cell, excited at the frequencies of the band-edge states. (e) Simulated displacement field for the interface state, excited by a plane-wave incidence. (f) Measured pressure amplitude near the interface as a function of frequency. The yellow region denotes the band gap. (g) Measured interface state distributions at a frequency of 0.331 MHz.

The topological property of the acoustic waveguide can be characterized by the Zak phase. The simulated dispersions of the water waveguide sandwiched by the walls of steel-air metastructures are shown in Fig. 3(a). As expected, there is no other mode in the band gap. Note that for specific parameters, the metastructures can host topologically trivial defect modes in the waveguide, which, however, are sensitive to geometry parameters and can be removed from the band gap. For the lower band, the band-edge states at the center and boundaries of the first Brillouin zone are denoted by red and blue dots, respectively. Their acoustic pressure distributions are depicted in Fig. 3(b). The two states have different parity with respect to the center of the unit cell, indicating a nontrivial Zak phase of π . This property can also be demonstrated in experiment by measuring the acoustic pressure distributions in the waveguide under excitations at the band-edge frequencies. We select in the waveguide a unit cell with the x coordinate from 57.75 to 68.75 mm (the left edge of the waveguide is set to $x = 0$ mm). The simulated and measured results at the middle lines are exhibited in Figs. 3(c) and 3(d), which agree well with each other and consistently manifest the different parity features for the band-edge states.

With the nontrivial Zak phase, an interface state arises and is detectable when the excitation is at the interface state frequency within the band gap. The simulated displacement field under this excitation is provided in Fig. 3(e), which shows the field in the water waveguide is highly localized near the interface. In comparison, the field in the solid part is nearly negligible, which means the steel-air metastructure works well and screens all the solid modes. We measure the response spectra of the interface

state by inserting the pinducer at the interface. As shown in Fig. 3(f), the measured spectra reach a peak at around 0.331 MHz within the frequency band gap (marked as the yellow region). This peak frequency corresponds to that of the interface state. We further measure the spatial distribution of pressure field at this frequency. The result is shown in Fig. 3(g), where the pressure amplitude decays rapidly away from the interface point (at $x = 132$ mm).

Finally, we experimentally study the influence of disorder. As shown in Fig. 4(a), six steel sheets (marked as red) are stuck randomly to the walls of the waveguide to change its width. The measured amplitude response spectra of the sample with the disorder are shown in Fig. 4(b), where the peak of the interface state in the band gap is robust to the disorder. The corresponding pressure field distribution of the interface state is exhibited in Fig. 4(b) and shows localization at the interface point.

IV. CONCLUSION

In summary, we realize a 1D waterborne acoustic waveguide. We experimentally measure the nonzero Zak phase and observe the topological interface state and its robustness against disorder. In our design, a steel-air metastructure is used to open a wide and high frequency band gap that screens the unwanted solid modes, providing a strategy to observe topological states in water. The robustness of the topological states in water provides possible applications to versatile usages such as waterborne acoustic field manipulations, sonar sensors, and noninvasive acoustic tweezers.

ACKNOWLEDGMENTS

This work is supported by the National Key R&D Program of China (Grants No. 2022YFA1404900 and No. 2022YFA1404500), the National Natural Science Foundation of China (Grants No. 11890701, No. 11974262, No. 11974005, No. 12004286, No. 12104347, and No. 12222405).

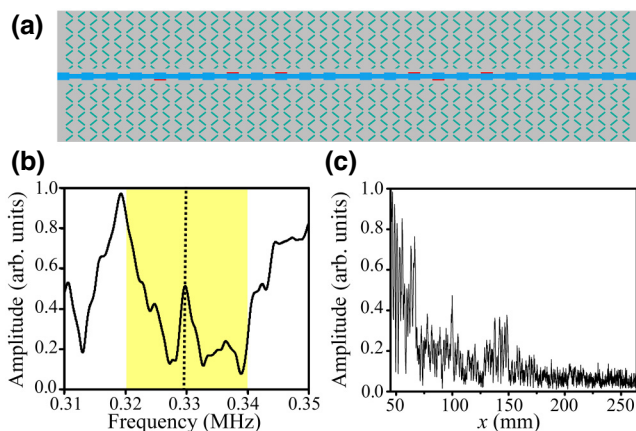


FIG. 4. (a) Schematic of the supercell with disorder. The red bars represent the steel sheets serving as the introduced disorder. (b) Measured pressure amplitude near the interface as a function of frequency. The yellow region denotes the band gap. (c) Measured interface state distribution at a frequency of 0.329 MHz.

- [1] M. Z. Hasan and C. L. Kane, Colloquium: Topological insulators, *Rev. Mod. Phys.* **82**, 3045 (2010).
- [2] S. H. Mousavi, A. B. Khanikaev, and Z. Wang, Topologically protected elastic waves in phononic metamaterials, *Nat. Commun.* **6**, 8682 (2015).
- [3] R. Fleury, A. B. Khanikaev, and A. Alu, Floquet topological insulators for sound, *Nat. Commun.* **7**, 11744 (2016).
- [4] C. He, S. Y. Yu, H. Wang, H. Ge, J. Ruan, H. Zhang, M. H. Lu, and Y. F. Chen, Hybrid acoustic topological insulator in three dimensions, *Phys. Rev. Lett.* **123**, 195503 (2019).
- [5] Y. Shen, C. Qiu, X. Cai, L. Ye, J. Lu, M. Ke, and Z. Liu, Valley-projected edge modes observed in underwater sonic crystals, *Appl. Phys. Lett.* **114**, 023501 (2019).

- [6] M. Wang, W. Zhou, L. Bi, C. Qiu, M. Ke, and Z. Liu, Valley-locked waveguide transport in acoustic heterostructures, *Nat. Commun.* **11**, 3000 (2020).
- [7] Y. Yang, Z. Gao, H. Xue, L. Zhang, M. He, Z. Yang, R. Singh, Y. Chong, B. Zhang, and H. Chen, Realization of a three-dimensional photonic topological insulator, *Nature* **565**, 622 (2019).
- [8] Y. Li, Y. Yu, F. Liu, B. Zhang, and G. Shvets, Topology-controlled photonic cavity based on the near-conservation of the valley degree of freedom, *Phys. Rev. Lett.* **125**, 213902 (2020).
- [9] G. G. Liu, Z. Gao, Q. Wang, X. Xi, Y. H. Hu, M. Wang, C. Liu, X. Lin, L. Deng, S. A. Yang, P. Zhou, Y. Yang, Y. Chong, and B. Zhang, Topological Chern vectors in three-dimensional photonic crystals, *Nature* **609**, 925 (2022).
- [10] C. L. Kane and T. C. Lubensky, Topological boundary modes in isostatic lattices, *Nat. Phys.* **10**, 39 (2013).
- [11] L. M. Nash, D. Kleckner, A. Read, V. Vitelli, A. M. Turner, and W. T. Irvine, Topological mechanics of gyroscopic metamaterials, *Proc. Natl. Acad. Sci. U. S. A.* **112**, 14495 (2015).
- [12] J. Attig, K. Roychowdhury, M. J. Lawler, and S. Trebst, Topological mechanics from supersymmetry, *Phys. Rev. Res.* **1**, 032047(R) (2019).
- [13] Z. Yang, F. Gao, X. Shi, X. Lin, Z. Gao, Y. Chong, and B. Zhang, Topological acoustics, *Phys. Rev. Lett.* **114**, 114301 (2015).
- [14] Y. Ding, Y. Peng, Y. Zhu, X. Fan, J. Yang, B. Liang, X. Zhu, X. Wan, and J. Cheng, Experimental demonstration of acoustic Chern insulators, *Phys. Rev. Lett.* **122**, 014302 (2019).
- [15] H. Xue, Y. Yang, F. Gao, Y. Chong, and B. Zhang, Acoustic higher-order topological insulator on a kagome lattice, *Nat. Mater.* **18**, 108 (2019).
- [16] X. Ni, M. Li, M. Weiner, A. Alu, and A. B. Khanikaev, Demonstration of a quantized acoustic octupole topological insulator, *Nat. Commun.* **11**, 2108 (2020).
- [17] L. Yang, Y. Wang, Y. Meng, Z. Zhu, X. Xi, B. Yan, S. Lin, J. Chen, B. Shi, Y. Ge, S. Yuan, H. Chen, H. Sun, G. Liu, Y. Yang, and Z. Gao, Observation of Dirac hierarchy in three-dimensional acoustic topological insulators, *Phys. Rev. Lett.* **129**, 125502 (2022).
- [18] T. Wang, M. Ke, S. Xu, J. Feng, C. Qiu, and Z. Liu, Dexterous acoustic trapping and patterning of particles assisted by phononic crystal plate, *Appl. Phys. Lett.* **106**, 163504 (2015).
- [19] H. Dai, B. Xia, and D. Yu, Microparticles separation using acoustic topological insulators, *Appl. Phys. Lett.* **119**, 111601 (2021).
- [20] J. Li, A. Crivoi, X. Peng, L. Shen, Y. Pu, Z. Fan, and S. A. Cummer, Three dimensional acoustic tweezers with vortex streaming, *Commun. Phys.* **4**, 113 (2021).
- [21] J. Li, C. Shen, T. J. Huang, and S. A. Cummer, Acoustic tweezer with complex boundary-free trapping and transport channel controlled by shadow waveguides, *Sci. Adv.* **7**, eabi5502 (2021).
- [22] P. Liu, H. Li, Z. Zhou, and Y. Pei, Topological acoustic tweezer and pseudo-spin states of acoustic topological insulators, *Appl. Phys. Lett.* **120**, 222202 (2022).
- [23] M. A. Ghanem, A. D. Maxwell, Y. N. Wang, B. W. Cunitz, V. A. Khokhlova, O. A. Sapozhnikov, and M. R. Bailey, Noninvasive acoustic manipulation of objects in a living body, *Proc Natl. Acad. Sci. U. S. A.* **117**, 16848 (2020).
- [24] A. J. Heeger, S. Kivelson, J. R. Schrieffer, and W. P. Su, Solitons in conducting polymers, *Rev. Mod. Phys.* **60**, 781 (1988).
- [25] Z. Yang and B. Zhang, Acoustic type-II Weyl nodes from stacking dimerized chains, *Phys. Rev. Lett.* **117**, 224301 (2016).
- [26] H. Xue, Y. Yang, G. Liu, F. Gao, Y. Chong, and B. Zhang, Realization of an acoustic third-order topological insulator, *Phys. Rev. Lett.* **122**, 244301 (2019).
- [27] Z.-G. Chen, L. Wang, G. Zhang, and G. Ma, Chiral symmetry breaking of tight-binding models in coupled acoustic-cavity systems, *Phys. Rev. Appl.* **14**, 024023 (2020).
- [28] Y. X. Shen, L. S. Zeng, Z. G. Geng, D. G. Zhao, Y. G. Peng, and X. F. Zhu, Acoustic adiabatic propagation based on topological pumping in a coupled multicavity chain lattice, *Phys. Rev. Appl.* **14**, 014043 (2020).
- [29] M. Xiao, Z. Q. Zhang, and C. T. Chan, Surface impedance and bulk band geometric phases in one-dimensional systems, *Phys. Rev. X* **4**, 021017 (2014).
- [30] W. Y. Zhang, H. Chen, H. S. Lai, J. L. Xie, C. He, and Y. F. Chen, Multimode topological interface states in a one-dimensional elastic-wave phononic crystal, *Phys. Lett. A* **479**, 128929 (2023).
- [31] X. Hu, Z. Hang, J. Li, J. Zi, and C. T. Chan, Anomalous Doppler effects in phononic band gaps, *Phys. Rev. E* **73**, 015602 (2006).
- [32] M. Xiao, G. Ma, Z. Yang, P. Sheng, Z. Q. Zhang, and C. T. Chan, Geometric phase and band inversion in periodic acoustic systems, *Nat. Phys.* **11**, 240 (2015).
- [33] D. J. Apigo, W. Cheng, K. F. Dobiszewski, E. Prodan, and C. Prodan, Observation of topological edge modes in a quasiperiodic acoustic waveguide, *Phys. Rev. Lett.* **122**, 095501 (2019).
- [34] Q. Li, X. Xiang, L. Wang, Y. Huang, and X. Wu, Topological ventilated sound switch from acoustic Su-Schrieffer-Heeger model, *Appl. Phys. Lett.* **122**, 191704 (2023).
- [35] A. Coutant, A. Sivadon, L. Zheng, V. Achilleos, O. Richoux, G. Theocharis, and V. Pagneux, Acoustic Su-Schrieffer-Heeger lattice: Direct mapping of acoustic waveguides to the Su-Schrieffer-Heeger model, *Phys. Rev. B* **103**, 224309 (2021).
- [36] X. Zhang, H. X. Wang, Z. K. Lin, Y. Tian, B. Xie, M. H. Lu, Y. F. Chen, and J. H. Jiang, Second-order topology and multidimensional topological transitions in sonic crystals, *Nat. Phys.* **15**, 582 (2019).
- [37] Z. Xiong, Z. K. Lin, H. X. Wang, X. Zhang, M. H. Lu, Y. F. Chen, and J. H. Jiang, Corner states and topological transitions in two-dimensional higher-order topological sonic crystals with inversion symmetry, *Phys. Rev. B* **102**, 125144 (2020).